Bates College
SCARAB

All Faculty Scholarship | Departments and Programs

9-8-2020

Lattice Anharmonicity of Stereochemically Active Lone Pairs Controls Thermochromic Band Gap Reduction of $PbVO_3Cl$

Uyen Dang
The University of Texas at Arlington

Wasif Zaheer
Texas A&M University

Wuyue Zhou
Bates College

Anna Kandel
Bates College

Melissa Orr
The University of Texas at Arlington

See next page for additional authors

Follow this and additional works at: https://scarab.bates.edu/faculty_publications

Recommended Citation

Uyen Dang, Wasif Zaheer, Wuyue Zhou, Anna Kandel, Melissa Orr, Richard W. Schwenz, Geneva Laurita, Sarbajit Banerjee, and Robin T. Macaluso. (2020) Lattice Anharmonicity of Stereochemically Active Lone Pairs Controls Thermochromic Band Gap Reduction of PbVO3Cl. Chemistry of Materials. 32(17). 7404-7412. https://doi.org/10.1021/acs.chemmater.0c02342

This Article is brought to you for free and open access by the Departments and Programs at SCARAB. It has been accepted for inclusion in All Faculty Scholarship by an authorized administrator of SCARAB. For more information, please contact batesscarab@bates.edu.

Authors

Uyen Dang, Wasif Zaheer, Wuyue Zhou, Anna Kandel, Melissa Orr, Richard W. Schwenz, Geneva Laurita, Sarbajit Banerjee, and Robin T. MacAluso

This article is available at SCARAB: https://scarab.bates.edu/faculty_publications/204

Lattice Anharmonicity of Stereochemically Active Lone Pairs Controls Thermochromic Band Gap Reduction of $PbVO_3Cl$

Uyen Dang,[a,#] Wasif Zaheer,[b,#] Wuyue Zhou,[c] Anna Kandel,[c] Melissa Orr,[a] Richard W. Schwenz,[d] Geneva Laurita,[c] Sarbajit Banerjee,[b] Robin T. Macaluso[a,*]

[a] Department of Chemistry and Biochemistry, University of Texas at Arlington, Arlington, TX 76019

[b] Department of Chemistry, Texas A & M University, College Station, TX

[c] Department of Chemistry and Biochemistry, Bates College, Lewiston, ME 04240

[d] Department of Chemistry and Biochemistry, University of Northern Colorado, Greeley, CO 80639

[#] Equal authorship

*Corresponding Author. E-mail: robin.macaluso@uta.edu

Abstract

Stereochemical active lone pairs of electrons in plays an important role in diverse range of physical phenomena in a plethora of materials, ranging from semiconducting halide perovskites to thermochromic inorganic-organic hybrids. In this paper, we demonstrate the importance of the $6s^2$ lone pair on the reversible thermochromic transition in the mixed-anion inorganic compound, $PbVO_3Cl$. This $6s^2$ stereochemically active lone pair results in subtle structural distortions upon heating while maintaining its overall orthorhombic structure. These distortions result in competing interactions with the Pb $6s^2$ lone pair and ultimately, a pronounced change between yellow and red at ~200 °C. X-ray diffraction analyses of $PbVO_3Cl$ demonstrates two-dimensional features in contrast to the three-dimensional network in isostructural $BaVO_3Cl$. X-ray and neutron pair distribution function experiments reveal that Pb-O interatomic distances decrease upon heating, while Pb-Cl distances are only affected by thermal motion. X-ray photoelectron spectroscopy measurements provide experimental evidence of the presence of the $6s^2$ lone pair at the valence band maximum, which are corroborated by first-principles calculations. The results demonstrate a broadly generalizable mechanism for using repulsions between lone-pair electrons of p-block cations to drive discontinuous changes of local symmetry and electronic structure.

Introduction

Mixed-anion systems, e.g., oxynitrides, oxysulfides and oxyhalides, stand out as a class of materials because of the tunability of atomic and electronic structure and therefore, semiconducting band gaps.[1-4] Mixed-anion systems containing stereochemically active lone pairs are particularly interesting because structural distortions associated with the lone pairs contribute to magnetic,[5] photocatalytic,[3] and nonlinear optical behavior.[6-8] Comparing $PbBi_2OX$ (X = Cl, Br, I) to $AEBi_2OCl$ (AE = Sr, Ba) demonstrated that the hybridization between the $6s^2$ lone pair and O $2p$ resulted in an upward shift of the valence band (VB) in $PbBi_2OX$ (X = Cl, Br, I), thereby making it a potential visible light-induced water splitting catalyst.[3] Thermochromic transitions due to disorder associated with $5s^2$ lone pairs have been recently described for the organic-inorganic hybrid (2-MIm)SbI_4 (MIm – methylimidiazolium).[9] However, lone-pair-driven electronic instabilities bringing about a pronounced modulation of electronic structure are much less explored in all-inorganic systems.

Stereochemically active lone pairs derived from p-block cations have long been understood to affect structural distortions.[10] It is important to point out that in inorganic solids, stability of structural distortions associated with stereochemically active lone pairs are closely connected to lone pair-anion interactions.[11] For example, in the halide perovskite, $CsSnBr_3$, small, localized distortions invoked by the Sn $5s$-Br $4p$ interactions play an important role in dielectric and optical behavior.[12] The unusual band gap widening with temperature of PbS, PbSe and PbTe semiconductors has also been attributed to the emphanisis effect, in which the Pb^{2+} lone pairs become stereochemically active upon warming, leading to local distortions at elevated temperatures.[13-15] The link between lone pair-anion interactions to structural distortion is strongly justified by the combination of experimental spectroscopic evidence and theoretical revised lone pair model,[10, 16] leading to promising predictive abilities in the area of catalysis. For instance, the hybridization of Pb $6s^2$ or Sn $5s^2$ states with O $2p$ states in β-$Pb_xV_2O_5$ and β-$Sn_xV_2O_5$ yields a combination of occupied bonding and anti-bonding lone-pair—anion states. The latter is further stabilized by mixing with unoccupied cation 5 and 6 p-states, yielding an occupied hybrid "mid-gap" state above the O $2p$ valence band[2, 17, 18] with a distinctive spectroscopic signature distinguishable by hard X-ray photoemission spectroscopy. Such lone-pair-derived mid-gap states have been utilized to extract holes from photoexcited II-VI quantum dots, enabling the design of heterostructures for water splitting and mitigating the longstanding challenge of photo-anodic corrosion of chalcogenide quantum dots that has limited their use in photocatalysis.

This paper establishes the unique effect of thermally induced structural distortions derived from a stereochemically active lone pair on a thermochromic transition in the mixed-anion inorganic compound, $PbVO_3Cl$. Previous work on this material was motivated by the Pb $6s^2$ lone pairs.[19] Unlike other mixed anion compounds containing lone pairs where the harder cation interacts with the oxide while the softer metal interacts with the softer anion, e.g., chalcogenide or halide, the $6s^2$ lone pairs in $PbVO_3Cl$ simultaneously interact with O and Cl, and thus $PbVO_3Cl$ presents a special opportunity to evaluate structural stability of lone pair interactions with anions of very different electronegativities. We show that thermally driven electrostatic repulsions between stereochemically active lone pairs on $PbCl_4$ units and the concomitant lattice distortion alters the hybridization of Pb $6s^2$ lone pair states with O $2p$ states, resulting in a thermochromic transition at ~200°C, which brings about a reversible color change between yellow and red because of local distortions of the atomic structure strongly coupled with modulation of the electronic structure. $BaVO_3Cl$, which does not contain a stereochemically active lone pair of electrons, was also prepared as a control for the comparison of the local structure of the two compounds. Total X-ray and neutron scattering were used to elucidate long and short-range crystal structures as a function of temperature. Density functional theory (DFT) calculations in conjunction with X-ray absorption near-edge structure (XANES) and hard X-ray spectroscopies (HAXPES) provide theoretical and experimental evidence of the key involvement of the Pb $6s^2$ lone pair in the electronic structure of $PbVO_3Cl$.

Materials and methods

Synthesis.

Powder samples of $PbVO_3Cl$ were prepared in a manner similar to procedures described elsewhere.[19] A mixture of PbO, $PbCl_2$, and V_2O_5 in a 1:1:1 molar ratio was ground in an agate mortar and pestle. The powders were pressed into a pellet and placed inside a fused silica ampoule. The ampoule was subsequently sealed under vacuum, heated at 3 °C/min to 450 °C, where it dwelled for 12 hours, and then cooled to 25 °C at 3 °C/min. The product was visibly yellow with a typical yield of ~86%. The impurity was found to be $PbCl_2$ which could be removed by washing the sample with DI water.

The synthesis of $BaVO_3Cl$ was based on a previously reported two-step procedure.[20] First, V_2O_5 and $BaCO_3$ were ground in an agate mortar and pestle and placed in a platinum crucible. The mixture was heated at 5.6 °C/min to 700 °C, where it dwelled for 6 hours, and then cooled to 25 °C

at 5.6 °C/min to yield BaV_2O_6. In the second step, a mixture of $BaCl_2$ and BaV_2O_6 in a 1:1 molar ratio was ground, pressed into pellet, placed in a fused silica ampoule and sealed under vacuum. The sample was heated at 30 °C/h to 480 °C, where it dwelled for 24 hours and then cooled at 8 °C/h down to 300 °C. The ampoule was removed from the furnace and quenched in an ice bath. The powder product was visible yellow with typical yields determined by X-ray powder diffraction of ~91% to ~94%.

Structural Characterization

Powder X-ray Diffraction

Powder X-ray diffraction (XRD) data were collected using a PANalytical Empyrean diffractometer equipped with a PIXcel^{3D} detector and Cu (λ = 1.5405980 Å) tube, which was operated at 45 kV and 40 mA. Data were collected over the angular range $10° \leq 2\theta \leq 90°$ with a step width of 0.008° and step rate of 0.0557 °/s at room temperature. The background was estimated by a polynomial function varying four coefficients. Atomic coordinates, scale factor, peak shape function (U, V, W), and isotropic displacement parameters were refined.

Total Scattering Measurements

Time-of-flight (TOF) neutron scattering data were collected at 100, 300, and 500 K on the nanoscale ordered materials diffractometer (NOMAD) diffractometer at the Spallation Neutron Source (SNS), Oak Ridge National Laboratory (ORNL) with a collection time of approximately 2 to 4 h per sample.[21] The samples were loaded into quartz capillaries and an empty capillary was subtracted as background. The pair distribution functions (PDF), *G(r),* were obtained by the transformation of the normalized total scattering function, *S(Q)*, with a Q_{max} = 28.0 Å^{-1}.

Synchrotron X-ray total scattering measurements were collected on the 11-ID-B beamline at the Advanced Photon Source (APS) located at Argonne National Laboratory (ANL) with a photon wavelength of 0.1432 Å from 300 to 575 K. Samples of fine powder were transferred into a Kapton capillary (1.1 mm OD, 1.0 mm ID) tightly compacted by glass wool to ensure the maximum packing fraction. The two samples were separated in the capillary by glass wool. Data were collected every 2 min upon warming at a rate of 5 K min^{-1}. Corrections to obtain the *S(Q)* and subsequent Fourier transform with a Q_{max} of 27.55 Å^{-1} to obtain the *G(r)* was performed using the program PDFgetX2.[22] The local structure was investigated via analysis of the real-space PDF using the PDFgui software suite.[23] Crystal structures were visualized using the VESTA suite of programs.[24]

Density Functional Theory

First-principles calculations were performed using density functional theory, as implemented within the Vienna *ab initio* simulation package (VASP). The projector augmented wave (PAW) formalism was used to model electron−ion interactions.[28-30] A kinetic energy cutoff of 520 eV was used for plane-wave basis restriction. Electronic exchange and correlation effects were included using the generalized gradient approximation based on the Perdew−Burke−Ernzerhof functional (GGA-PBE).[31] The strong electronic correlation of the V 3*d* electrons was accounted for using a Hubbard correction U_{eff} = 3.25 eV.[32] Supercells with dimensions 2×2×1 were used to relax the $PbVO_3Cl$ and $BaVO_3Cl$ structures. A uniform Γ-centered 4 × 4 × 4 Monkhorst−Pack *k*-point grid was used for structure relaxations. For geometry optimization, the supercells were relaxed until the cartesian components of the forces were below ±0.01 eV·Å^{-1}.

Hard X-ray Photoelectron Spectroscopy

Valence band HAXPES measurements were performed at the National Institute of Standards and Technology beamline 7-ID-2 of the National Synchrotron Light Source II at the Brookhaven National Laboratory. Measurements at an incident photon energy of 2 keV were performed with a pass energy of 200 eV, whereas the measurements at the incident photon energy of 5 keV were collected at a pass energy of 500 eV. The data was collected with a step size of 0.85 eV and the analyzer axis oriented parallel with the photoelectron polarization vector. The higher excitation of HAXPES circumvents deleterious charging issues that are common to ultraviolet and soft X-ray photoelectron spectroscopy. Photon energy selection was accomplished using a double Si (111) crystal monochromator. No evidence of charging was observed during our measurements. The beam energy was aligned to the Fermi level of a silver foil before measurements.

X-ray Absorption Near-Edge Structure Spectroscopy

V L-edge and O K-edge measurements were performed at beamline 7-ID-1 of the National Synchrotron Light Source II of Brookhaven National Laboratory device beamline operated by the National Institute of Standards and Technology. A horizontally polarized x-ray beam with a spot size of 10 μm was used for data collection. A grid bias of -300 V was used to reduce the low-energy electrons and improve surface sensitivity. A charge compensation gun was used to avert the charging of the samples. The data was collected with a resolution of 0.5 eV for all plotted spectra. The partial electron yield signals were normalized to the incident beam intensity from a freshly evaporated gold mesh. The spectra were energy calibrated to O K-edge for a standard TiO_2 sample.

Results and Discussion

Average crystal structure

Both $PbVO_3Cl$ and $BaVO_3Cl$ adopt the orthorhombic *Pnma* space group, in agreement with previous structural reports.[19] Results from powder X-ray diffraction analyses of both compounds are provided in Tables S1 and S2. X-ray fluorescence results (Table S3) indicate 1 mol Pb:1 mol V ratio, in agreement with powder XRD.

Since $PbVO_3Cl$ and $BaVO_3Cl$ share the same space group and atomic positions, similarities in their crystal structures are to be expected. Their crystal structures are compared in Figures 1a and 1b. Both compounds include chains of edge-sharing VO_5 square pyramids running in the *b* direction. Square pyramids within a chain are in a *trans*-configuration in which the apical oxygen points alternately in the *ac* plane as shown in Figure 1a. The VO_5 square pyramids in both compounds are similarly distorted. The vanadium atom is slightly off-center in the VO_5 square pyramid with a short doubly bonded apical V-O bond (1.599 - 1.611 Å) and four long bonds of 1.824 - 1.920 Å and of 1.805 - 1.956 Å for Pb and Ba, respectively. These results agree with previous structural reports.[25]

In both compounds, the chains are connected by the divalent cation (Pb^{2+} or Ba^{2+}); however, the connectivity of Pb^{2+} is distinct from its Ba^{2+} counterpart. Each BaO_5Cl_4 polyhedron in $BaVO_3Cl$ connects to the oxygen atoms of three unique VO_5 square pyramids to form a three-dimensional network as shown in Figure 1b. In $PbVO_3Cl$, on the other hand, each PbO_3Cl_3 polyhedron connects two VO_5 square pyramids from two neighboring chains, resulting in two-dimensional sheets in the *bc* plane, with a clear separation between layers of ~3.3 Å. This interlayer separation and coordinate undersaturation of the main-group cation is diagnostic of the role of stereoactive lone pairs, which have an approximate volume of an oxide or fluoride ion

Coordination environments around the divalent cations in $PbVO_3Cl$ and $BaVO_3Cl$ are depicted in Figures 1c and 1d, respectively. The Pb^{2+} cation is coordinated by three oxygen atoms and three chlorine atoms while Ba^{2+} is linked to five oxygen atoms and four chlorine atoms. Two of the oxygen atoms also form one edge of the VO_5 square pyramid base. Their interatomic distances – Pb-O and Pb-Cl and to that of Ba-O and Ba-Cl –are slightly shorter than bond distances calculated by summing their radii, Pb^{2+} (1.19 Å), Ba^{2+}(1.47 Å), O^{2-} (1.40 Å) and Cl- (1.80 Å).[26]

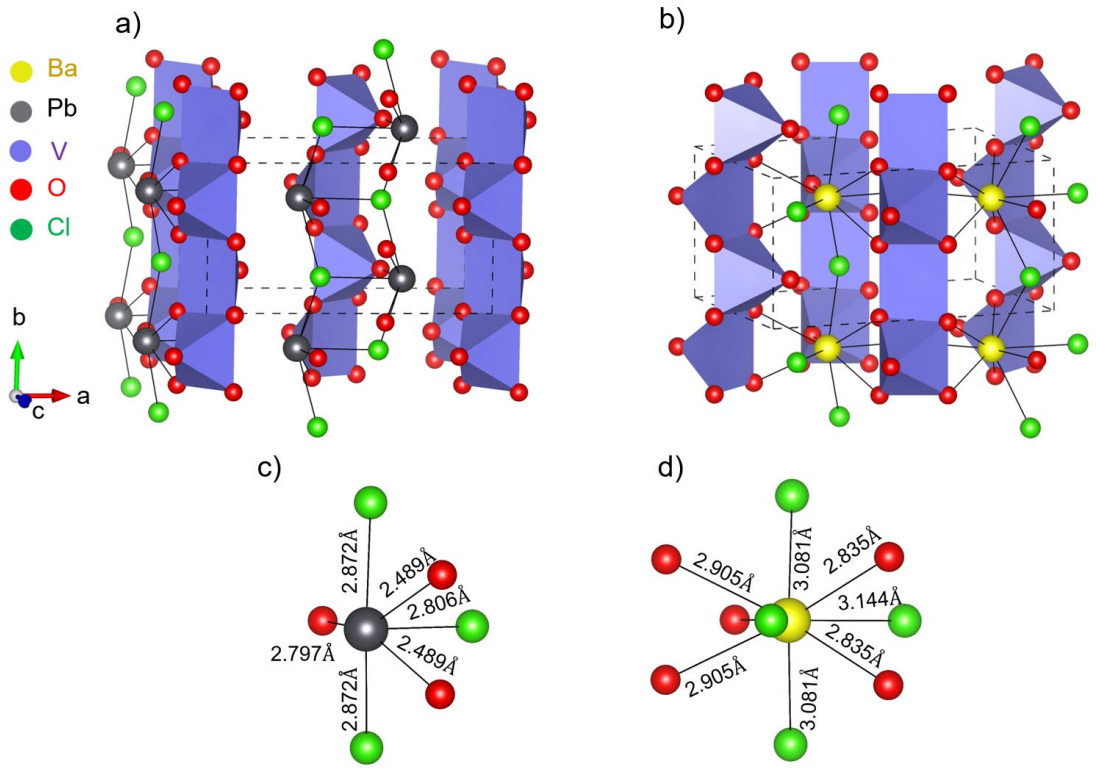

Figure 1: Average crystal structures of (a) $PbVO_3Cl$ and b) $BaVO_3Cl$. Local coordination environments and interatomic distances of the divalent cation environment in (c) PbO_3Cl_3 and (d) BaO_5Cl_4 at room temperature.

Total Scattering

To better understand the local structure of the two samples, analysis of the X-ray Pair Distribution Function (XPDF) was performed. The PDF is a histogram of all atom-atom correlations in material and incorporates both Bragg and diffuse scattering from a sample, representing the local bonding and atom-atom interactions. Therefore, by analysing how well (or how poorly) the XPDF data is fit by the crystallographic *Pnma* structure, we can understand deficiencies in the model in the form of structural disorder. Fits of XPDF data, provided in Figure 2, against the structural model based on conventional laboratory X-ray diffraction for $PbVO_3Cl$ and $BaVO_3Cl$ illustrate that the average *Pnma* structure more accurately describes the local structure for $BaVO_3Cl$. Although the XPDF data agree well with the average structural model for all temperatures (all R_w values are between 7-10% for the fits over and *r*-range of 1-6Å), the peaks at ~2.5 – 2.8 Å, which arise from Pb-O and Pb-Cl pair correlations, are poorly described by the average structural model for $PbVO_3Cl$ at all temperatures, indicating that there is more disorder in the local coordination of Pb than the average structure can describe. In $BaVO_3Cl$, the analogous peaks (at ~2.9 – 3.0 Å) peak shifts towards larger r as the temperature increases due to thermal expansion, yet the peak remains well fit. Pair correlations were

determined from the partial neutron and X-ray pair distribution functions (Figure S1). Additional fitting of the XPDF data over various length scales can be seen in Figures S2 and S3.

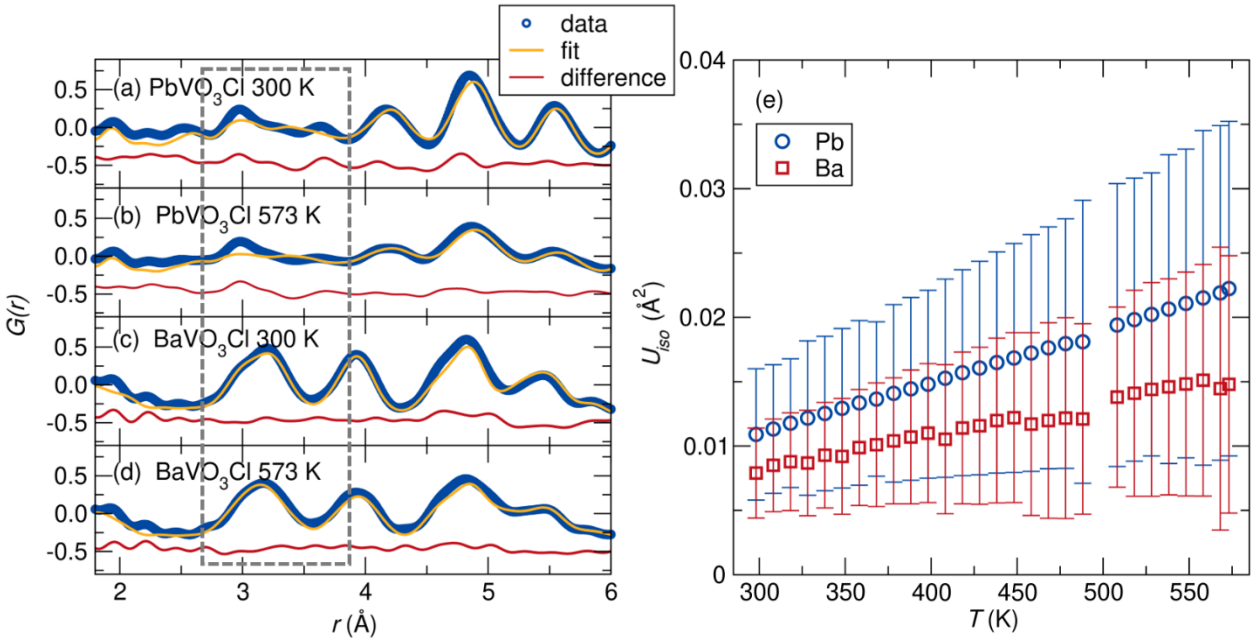

Figure 2: *Left:* Fits of XPDF data against the average *Pnma* structures for $PbVO_3Cl$ [(a) 300 K and (b) 573 K and $BaVOCl_3$ [(c) 300 K and (d) 573 K]. Peaks highlighted in the dashed box indicate regions where the data is poorly fit in the Pb-analogue. *Right:* Isotropic atomic displacement parameters (U_{iso}) of Pb and Ba from XPDF data Isotropic atomic displacement parameters (U_{iso}) of Pb and Ba from XPDF data

Atomic displacement parameters (ADP) provide insight into structural disorder. The unrealistically low U_{iso} of O1 obtained in our Rietveld refinements of powder X-ray diffraction data for $PbVO_3Cl$ (Table S2) may be attributed to the relatively low scattering power of O (compared to Pb) or local disorder. Hence, we were motivated to investigate ADPs using pair distribution function using X-ray and neutron total scattering. Isotropic ADPs (U_{iso}) of Pb and Ba as a function of temperature are shown in the right panel of Figure 2. The U_{iso} values increase with temperature as expected with increasing thermal motion. Three additional trends in Figure 2b indicate the presence of the lone pair: consistently higher U_{iso} values, larger error and faster rate of increase of U_{iso} for $PbVO_3Cl$ with temperature. Because Pb (Z = 82) possesses more electron density than Ba (Z = 56), it would be reasonable to anticipate that U_{iso} of Pb to be smaller than U_{iso} of Ba; however, we observe the opposite trends at all temperatures, posited to arise from additional disorder from the stereochemically active lone pair of Pb^{2+}. Figure 3 provides a closer view of evolution of the XPDF data upon warming. The peak at ~3.0 Å indicates the Pb/Ba--Cl bond (see Supplemental Figure S1 for partials), which remains relatively unchanged in shape upon warming. A large difference in peak

shape are the Pb-Pb and Ba-Ba correlations at ~5.5 Å. The Pb-Pb correlation develops a notable asymmetry in comparison to Ba-Ba correlations, indicating that the Pb displacements lack long-range correlation. This asymmetry becomes more pronounced at higher temperatures.

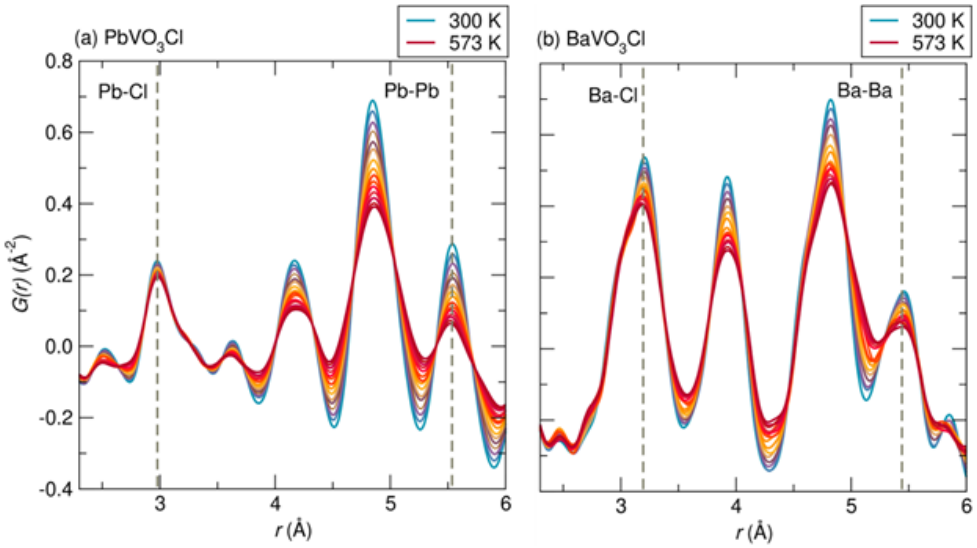

Figure 3: XPDF data for (a) $PbVO_3Cl$ and (b) $BaVO_3Cl$ indicate that the Pb-Cl and Ba-Cl peak shape (indicated by a dashed line) remains relatively unchanged with temperatures, whereas the Pb-Pb correlation (indicated by a dashed line) develop a distinct asymmetry upon warming, in contrast to the same Ba-Ba correlation in $BaVO_3Cl$.

Because oxygen is in the presence of lead with much higher scattering lengths via X-ray analysis, neutron pair distribution function (NPDF) data were collected to probe the oxygen environment. Fits of the neutron data against the *Pnma* structure can be found in Figure S4. Interestingly, the positive temperature dependence of the Pb U_{iso} (Figure 4) agrees with the trends observed in the XPDF data (Figure 2b); however, the temperature dependence of the O U_{iso} and Cl U_{iso} remain consistent across the temperature range (Figure 4). The right panel of Figure 4 provides intriguing insight into the dynamics of the crystal structure with temperature. We observe that while the VO_5 square pyramids expand with increasing temperature as expected, the Pb-O distance *decreases* with temperature and result in an overall smaller PbO_3Cl_3 polyhedra at higher temperatures. The Pb-Cl distance, however, is maintained at all temperatures, indicating that the primary structural effects on orbital overlap and thus observed physical properties are due to the changing Pb-O bond length. Therefore, the lone pair shifts towards oxygen are very subtle and that pair distribution function is essential to identifying the structural changes resulting from the presence of the $6s^2$ lone pair. The displacement of Pb is also temperature-dependent, and the Pb atoms shifts towards the 2D layer in which it already resides. While small-box modeling does provide insight into the presence of disorder

(observed as a poor fit by the crystallographic structure), it is noted that PDFgui applies a harmonic approximation and thus generates Gaussian peak shapes.[23] Therefore, as the lattice becomes more anharmonic as a result of the lone pair stereochemistry, a Gaussian peak becomes a less accurate model of the data, resulting in larger error in the fit parameters. The anisotropy of the disorder will be further investigated with temperature-dependent single crystal X-ray diffraction studies.

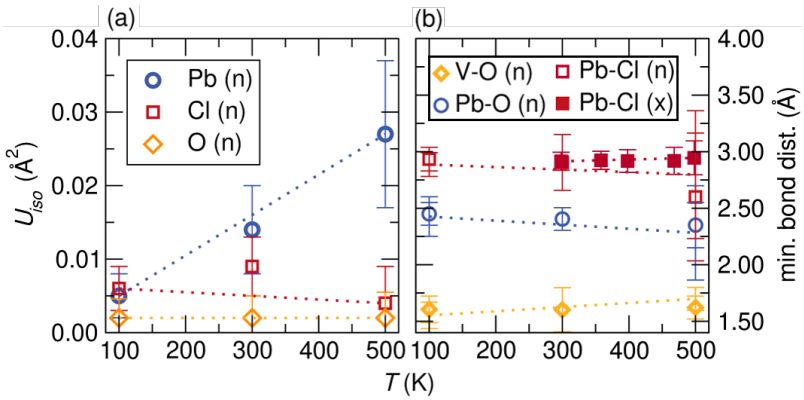

Figure 4: (a) Isotropic ADPs of Pb, Cl, and O and (b) V-O, Pb-O, and Pb-Cl distances with temperature

To probe the electronic structure origins of the differences in the local atomic structure of $PbVO_3Cl$ and $BaVO_3Cl$, HAXPES measurements have been performed at incident photon energies of 2.0 and 5.0 keV. In contrast to XPS, which primarily probes surface electronic structure, the high excitation energies accessible in HAXPES enable interrogation of the bulk electronic structure. HAXPES further serves as an excellent, and indeed, quantitative probe of orbital contributions at the valence band.[10, 18, 27] In general, photoionization cross-sections decay rapidly with an increase in incident photon energy; however, this effect is much more pronounced for subshells with higher orbital angular momentum.[33-35] Therefore, by varying the incident photon energy in photoemission experiments, the relative energy positioning and orbital contributions of states with *s*, *p*, and *d* character can be disentangled. Photoemission profiles obtained for both $PbVO_3Cl$ and $BaVO_3Cl$ at incident photon energies of 2.0 and 5.0 keV are plotted in Figures 5a and 5b.[10, 18, 27] A direct comparison of the photoemission spectra of $PbVO_3Cl$ and $BaVO_3Cl$ shows two major distinctions. First, a strong band centered at a binding energy of ~10.5 eV is observed for $PbVO_3Cl$ with no similar band for its *s*-block counterpart; the intensity of this feature increases with increasing incident photon energy, indicating the presence of electronic states with considerable Pb $6s^2$ character. Second, the valence band maximum of $PbVO_3Cl$ exhibits states higher up in energy that are not observed for $BaVO_3Cl$. These

states become more pronounced with an incident photon energy of 5.0 keV, again indicating their pronounced *s* character. The presence of these two features can be explained considering the revised lone pair model. The hybridization of the Pb $6s^2$ stereoactive lone pairs with O 2*p* and Cl 3*p* states leads to the formation of hybrid Pb 6*s* – O 2*p* and Pb 6*s* – Cl 3*p* bonding (B) and antibonding states (AB). The Pb 6*s* – O 2*p* and Pb 6*s* – Cl 3*p* bonding states collectively give rise to the feature observed at 10.5 eV in the valence band HAXPES spectra. The Pb 6*s* – O 2*p* and Pb 6*s* – Cl 3*p* antibonding states are further stabilized by an overlap with empty Pb 6*p* states in the conduction band wherein this

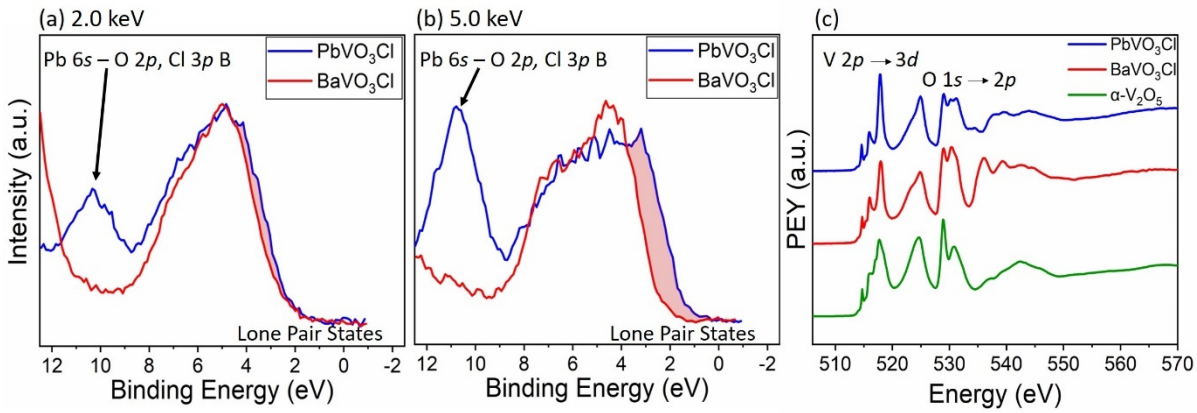

Figure 5: (a) HAXPES of $PbVO_3Cl$ and $BaVO_3Cl$ at an incident photon energy of 2.0 keV. (b) HAXPES of $PbVO_3Cl$ and $BaVO_3Cl$ at an incident photon energy of 5.0 keV. (c) XANES spectroscopy plots for α-V_2O_5, $BaVO_3Cl$ and $PbVO_3Cl$ at the V L-edge and O K-edge.

energetic stabilization drives a second-order Jahn—Teller distortion. The resulting hybrid states have considerable *s*-character, are situated at the valence band maximum, and have been represented as the shaded lone pair states in Figures 5a and 5b. Since O 2*p* states are closer in energy to Pb 6*s* states, greater mixing is expected in comparison to Cl 3*p* states, which induces a substantially greater splitting of B and AB states resulting in the Pb $6s^2$—O 2*p* states being positioned at the valence band maximum.

Electronic structure calculations were performed for both $BaVO_3Cl$ and $PbVO_3Cl$ to further understand the role of Pb $6s^2$ lone pair states in mediating the thermochromic transition. DFT is constrained in the treatment of strongly correlated systems because of band gap and localization errors, but the results nevertheless provide a guide to interpreting the origins and relative energy positioning of states observed in X-ray emission and absorption spectra. The projected density of states (PDOS) and total density of states (TDOS) for the ground state electronic structures of $BaVO_3Cl$ and $PbVO_3Cl$ are plotted in Figure 6. The PDOS of $BaVO_3Cl$ and $PbVO_3Cl$ indicates that in both compounds the valence band maximum primarily comprises contributions from Cl 3*p* and O

2*p* states, whereas the conduction band is derived primarily from V 3*d* states. In addition to Cl and O *p*-states, substantial contributions from Pb states, specifically Pb 6*s* and 6p_z states can also be observed at the top of the valence band maximum in $PbVO_3Cl$; no comparable contributions are discernible

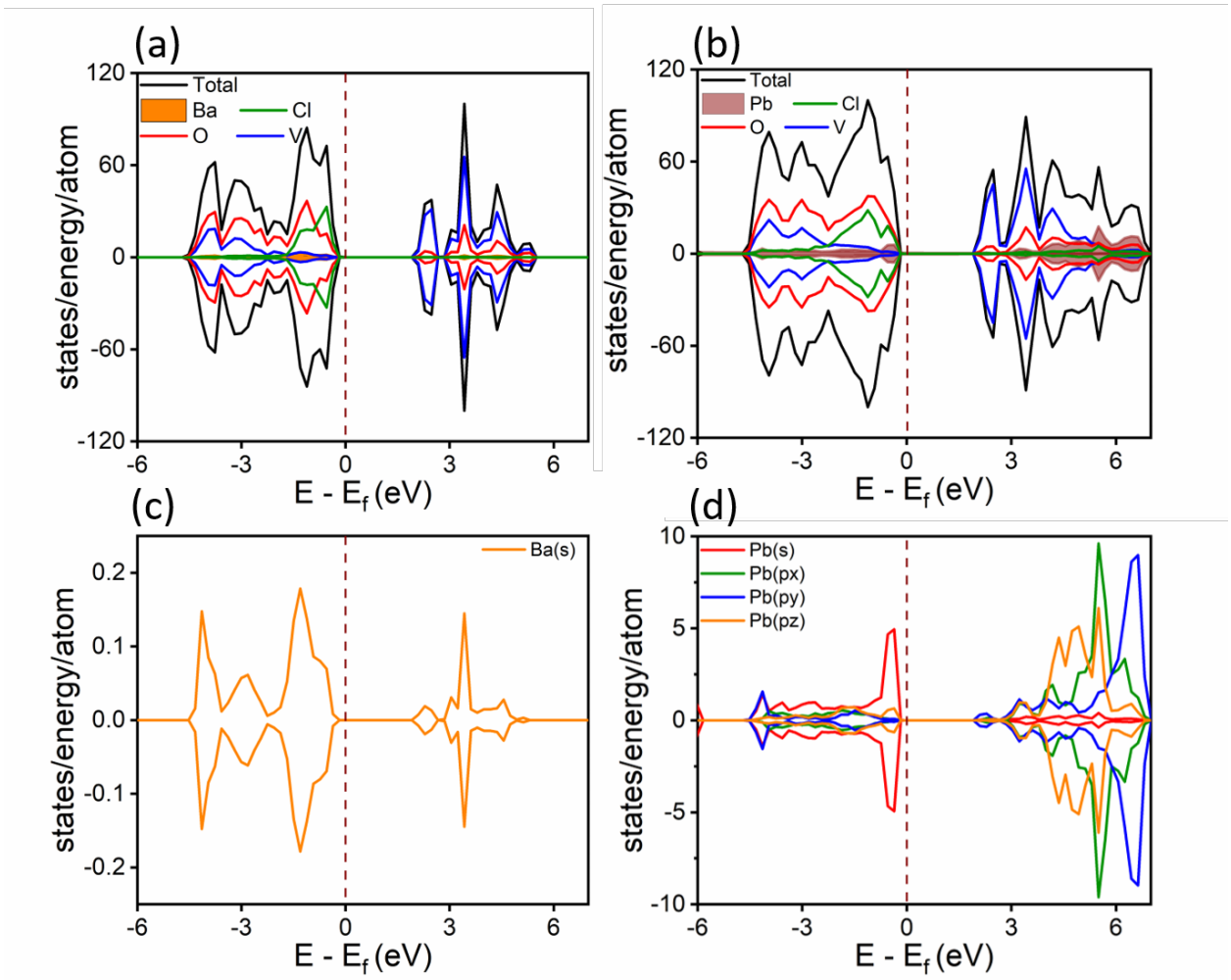

Figure 6: (a) GGA+U calculated ground state total density of states (TDOS) for $BaVO_3Cl$. (b) TDOS for $PbVO_3Cl$, Pb states are shaded in brown. (c) Calculated PDOS of Ba 6*s* in $BaVO_3Cl$. (d) PDOS of Pb 6s and 6p showing the presence of lone pair states at the VBM.

for the Ba analog. In other words, the DFT results corroborate the assignment of the HAXPES features at the top of the valence band as arising from states with considerable Pb $6s^2$ character.

XANES measurements were also performed at the V L-edge and O K-edge to map the conduction band of $BaVO_3Cl$ and $PbVO_3Cl$. XANES data for $BaVO_3Cl$ and $PbVO_3Cl$ are plotted in Figure 5c and compared with α-V_2O_5 where reliable assignments of the spectral features are available from excited state time-dependent DFT calculations.[28] The V L_{III}-edge is characterized by sharp

features corresponding to transitions from V 2*p* core states to V 3*d* states split by crystal field splitting in the square pyramidal coordination geometry.[29, 30] The V L_{II}-edge cannot be interpreted in terms of electronic structure as a result of spectral broadening derived from Coster-Kronig Auger decay processes. The O K-edge comprises transitions from O 1*s* core states to O 2*p* states hybridized with V 3*d* states that are split by crystal-field splitting. In accordance with our calculated PDOS for V in Figures S1a and S1b, the V L-edge XANES plots for $BaVO_3Cl$ and $PbVO_3Cl$ exhibit similar spectral features. Despite the similar VO_5 square pyramids observed in both $PbVO_3Cl$ and $BaVO_3Cl$, several finely structured features are observed in O K-edge spectra for the former that are not observed for the latter. Based on the DFT calculations, strong Pb 6*s* and 6*p* hybridization with O 2*p* states is expected (Figure 6d) and indeed these lone-pair hybridized states are clearly discernible in O K-edge spectra.

Lone pair states and concomitant structural distortions have been previously observed for lead oxides and chalcogenides as a result of the hybridization of unoccupied Pb 6*p* states with the antibonding states originating from the interaction of Pb 6*s* states with anion *p* states (Figure 7).[36, 37] However, in mixed-anion $PbVO_3Cl$, in addition to the Pb-O hybridization, the stereoactive lone pair states are also amenable to mixing with Cl states. Based on photoemission measurements, the Cl 3*p* (~6 eV) atomic states are higher in the valence band as compared to O 2*p* (~ 9eV) atomic states. The closer proximity of Pb 6s states with O 2p states facilitates improved hybridization and substantial *s*-character in hybrid B and AB states, which in turns promotes hybridization with Pb 6*p* states as sketched in Figure 7. Electronic structure calculations indicate Pb-O and Pb-Cl lone pair states are present at the valence band maximum (Figure 6b).

Conclusion

The change in color from yellow to red observed for $PbVO_3Cl$ above 200°C has no parallels in the alkaline-earth or rare-earth counterparts and suggests a thermally driven diminution of the bandgap. To understand the role of Pb $6s^2$ lone pairs in inducing a thermochromic transition in $PbVO_3Cl$, the coupling between geometric and electronic structure needs to be understood. The XPDF and NPDF analyses show that warming the $PbVO_3Cl$ sample leads to off-centering of the Pb atoms, likely because of lone-pair repulsions. The lattice anharmonicity arising from the Pb displacement brings the Pb and O atoms closer, whereas, the Pb—Cl distances remain essentially unchanged. The stronger Pb—O interactions suggest improved mixing of Pb $6s^2$ and O 2*p* states, resulting in greater splitting of the B and AB states sketched in Figure 7. As a result, the occupied AB

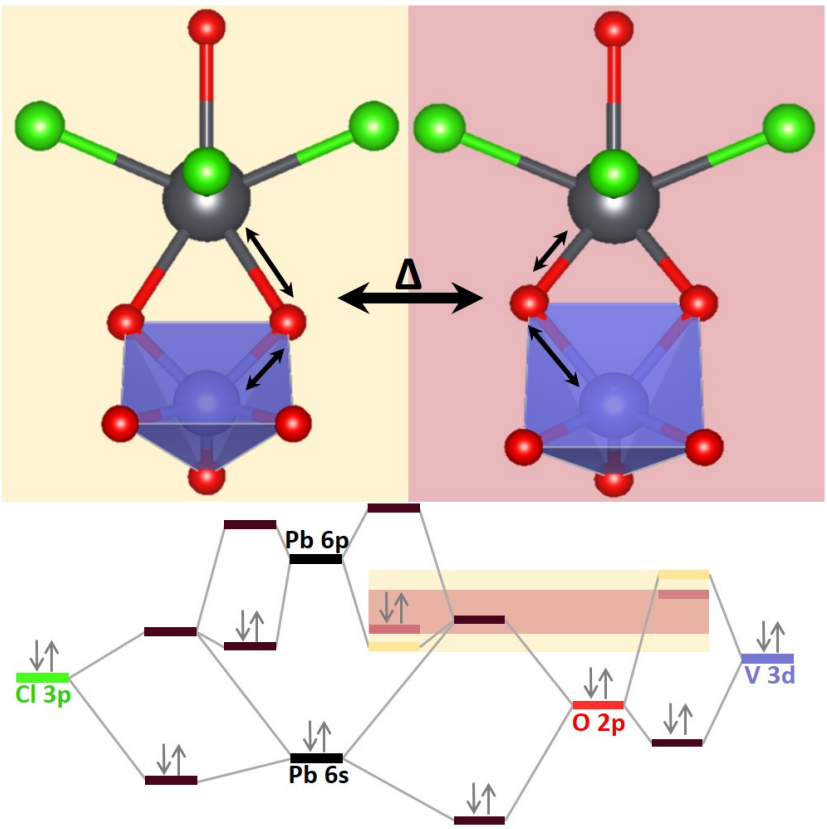

Figure 7: Pictorial representation of changes in the local geometric structure of Pb upon warming and its effects on the bandgap which enables the thermochromic transition in $PbVO_3Cl$. The Pb-O lone pair states constitute the HOMO (valence band maximum), whereas the empty V 3*d* – O 2*p* molecular states represent the LUMO (conduction band minimum.) The bandgap before and after the thermochromic transition is highlighted.

state will be positioned higher in energy, decreasing the effective bandgap of the system. A distinctive feature of V—O bonds in oxides is their highly tunable covalency/ionicity, which is manifested in the vast available array of binary vanadium oxide polymorphs.[31] The decreased bond length and increased hybridization of Pb—O states is furthermore compensated by an increase in V—O bond lengths and expansion of the VO_5 square pyramids, which is directly observed in the NPDF measurements. In other words, the lattice anharmonicity invoked by the anisotropic movement of Pb atoms because of lone pair repulsions strengthens Pb—O interactions and weakens V—O interactions. The diminished V 3d—O 2p hybridization furthermore reduces the splitting of the O 2p-derived valence band and the V 3d-derived conduction band. As sketched in Figure 10, the effective bandgap shrinks because of the shifting of Pb $6s^2$—O 2p hybrid anti-bonding states to higher energies and the accompanying shift of the V 3d—O2p hybridized conduction band edge to lower energies. The lone-pair driven structural distortions resulting in hybridization between a lone pair and O 2*p* and the covalency between the transition metal and O 2*p* are reminiscent of $BiMnO_3$.[32, 33] The strongly correlated changes

in lattice and electronic structure thus synergistically drive a decrease of the effective bandgap of $PbVO_3Cl$ resulting in a thermochromic transition from yellow to red at 200 °C.

Acknowledgements

RM and UD acknowledge support from UTA Startup funds, and UD acknowledges Sigma Xi Grant-in-Aid #G20191001100810061for support. WZ and SB acknowledge support from the National Science Foundation under DMR 1627197. DFT simulations were performed as part of a User Project at The Molecular Foundry (TMF), Lawrence Berkeley National Laboratory. T.M.F. is supported by the Office of Science, Office of Basic Energy Sciences, of the U.S. Department of Energy, under Contract No. DE-AC02- 05CH11231. This research used resources of the National Synchrotron Light Source II, a U.S. Department of Energy (DOE) Office of Science User Facility operated for the DOE Office of Science by Brookhaven National Laboratory under Contract No. DE-SC0012704. WZ acknowledges support from the Advanced Light Source (ALS) doctoral fellowship in residence. Acknowledgment is made to Bates College Startup funds (WZ, AK,and GL) for support of this research. GL would like to thank Hayden A. Evans for helpful discussions. A portion of this research used resources at the Spallation Neutron Source, a DOE Office of Science User Facility operated by the Oak Ridge National Laboratory. Use of the Advanced Photon Source at Argonne National Laboratory was supported by the U. S. Department of Energy, Office of Science, Office of Basic Energy Sciences, under Contract No. DE-AC02-06CH11357.

References

1. Jansen, M.; Letschert, H. P., Inorganic Yellow-Red Pigments without Toxic Metals. *Nature* **2000,** *404*, 980-982.
2. Cho, J. S., A.; Suwandaratne, N.; Wangoh, L.; Andrews, J. L.; Zhang, P.; Piper, L. F. J.; Watson, D. F.; Banerjee, S. , The Middle Road Less Taken: Electronic-Structure-Inspired Design of Hybrid Photocatalytic Platforms for Solar Fuel Generation. *Acc. Chem. Res.* **2019,** *52*, 645-655.
3. Suzuki, H.; Kunioku, H.; Higashi, M.; Tomita, O.; Kato, D.; Kageyama, H.; Abe, R., Lead Bismuth Oxyhalides $Pbbio_2x$ (X = Cl, Br) as Visible-Light-Responsive Photocatalysts for Water Oxidation: Role of Lone-Pair Electrons in Valence Band Engineering. *Chem. Mater.* **2018,** *30*, 5862-5869.
4. Kageyama, H.; Hayashi, K.; Maeda, K.; Attfield, J. P.; Hiroi, Z.; Rondinelli, J. M.; Poeppelmeier, K. R., Expanding Frontiers in Materials Chemistry and Physics with Multiple Anions. *Nat. Comm.* **2018,** *9*, 772.
5. Huang, X.; Zeng, Z.; Zhang, H., Metal Dichalcogenide Nanosheets: Preparation, Properties and Applications. *Chem. Soc. Rev.* **2013,** *42*, 1934-1946.
6. Cheng, W.-D.; Lin, C.-S.; Luo, Z.-Z.; Zhang, H., Designing the Syntheses and Photophysical Simulations of Noncentrosymmetric Compounds. *Inorganic Chemistry Frontiers* **2015,** *2*, 95-107.
7. Li, Y.-Y.; Wang, W.-J.; Wang, H.; Lin, H.; Wu, L.-M., Mixed-Anion Inorganic Compounds: A Favorable Candidate for Infrared Nonlinear Optical Materials. *Cryst. Growth Des.* **2019,** *19*, 4172-4192.
8. Yang, Z.; Hu, C.; Mutailipu, M.; Sun, Y.; Wu, K.; Zhang, M.; Pan, S., Oxyhalides: Prospecting Ore for Optical Functional Materials with Large Laser Damage Thresholds. *J. Mat. Chem.* **2018,** *6*, 2435-2442.
9. Gągor, A.; Banach, G.; Węcławik, M.; Piecha-Bisiorek, A.; Jakubas, R., The Lone-Pair-Electron-Driven Phase Transition and Order–Disorder Processes in Thermochromic (2-Mim)Sbi_4 Organic–Inorganic Hybrid. *Dalt. Trans.* **2017,** *46*, 16605-16614.

10. Walsh, A.; Payne, D. J.; Egdell, R. G.; Watson, G. W., Stereochemistry of Post-Transition Metal Oxides: Revision of the Classical Lone Pair Model. *Chem. Soc. Rev.* **2011,** *40*, 4455-4463.
11. Waghmare, U. V.; Spaldin, N. A.; Kandpal, H. C.; Seshadri, R., First-Principles Indicators of Metallicity and Cation Off-Centricity in the Ib-Vi Rocksalt Chalcogenides of Divalent Ge, Sn, and Pb. *Phys. Rev. B* **2003,** *67*, 125111.
12. Fabini, D. H.; Laurita, G.; Bechtel, J. S.; Stoumpos, C. C.; Evans, H. A.; Kontos, A. G.; Raptis, Y. S.; Falaras, P.; Van der Ven, A.; Kanatzidis, M. G.; Seshadri, R., Dynamic Stereochemical Activity of the Sn^{2+} Lone Pair in Perovskite $Cssnbr_3$. *J Am Chem Soc* **2016,** *138*, 11820-11832.
13. Hu, Y. Z.; Zhang, H. B.; Chong, W. K.; Li, Y. X.; Ke, Y. J.; Ganguly, R.; Morris, S. A.; You, L.; Yu, T.; Sum, T. C.; Long, Y.; Fan, H. J., Molecular Engineering toward Coexistence of Dielectric and Optical Switch Behavior in Hybrid Perovskite Phase Transition Material. *J. Phys. Chem. A* **2018,** *122*, 6416-6423.
14. Jensen, K. M. Ø.; Božin, E. S.; Malliakas, C. D.; Stone, M. B.; Lumsden, M. D.; Kanatzidis, M. G.; Shapiro, S. M.; Billinge, S. J. L., Lattice Dynamics Reveals a Local Symmetry Breaking in the Emergent Dipole Phase of Pbte. *Phys. Rev. B* **2012,** *86*, 085313.
15. Walsh, A.; Watson, G. W., The Origin of the Stereochemically Active Pb(Ii) Lone Pair: Dft Calculations on Pbo and Pbs. *J. Solid State Chem.* **2005,** *178*, 1422-1428.
16. Walsh, A.; Watson, G. W., The Origin of the Stereochemically Active Pb(Ii) Lone Pair: Dft Calculations on Pbo and Pbs. *J. Solid State Chem.* **2005,** *178*, 1422-1428.
17. Andrews, J. L. C., J.; Wangoh, L.; Suwandaratne, N.; Sheng, A.; Chauhan, S.; Nieto, K.; Mohr, A.; Kadassery, K. J.; Popeil, M. R.; Thakur, P. K.; Sfeir, M.; Lacy, D. C.; Lee, T.-L.; Zhang, P.; Watson, D. F.; Piper, L. F. J.; Banerjee, S. , Hole Extraction by Design in Photocatalytic Architectures Interfacing Cdse Quantum Dots with Topochemically Stabilized Tin Vanadium Oxide. *J. Am. Chem. Soc.* **2018,** *140*, 17163–17174.
18. Razek, S. A. P., M. R.; Wangoh, L.; Rana, J., Suwandaratne, N., Andrews, J. L., Watson, D. F.; Banerjee, S., Piper, L. F. J., Designing Catalysts for Water Splitting Based on Electronic Structure Considerations. *Electronic Structure* **2020,** *2*, 1-26.
19. Jo, V.; Kim, M. K.; Shim, I. W.; Ok, K. M., Synthesis, Structure, and Characterization of a Layered Mixed Metal Oxychloride, $Pbvo_3cl$. *Bull. Korean Chem. Soc.* **2009,** *30*, 2145-2148.
20. Borel, M. M.; Chardon, J.; Leclaire, A.; Raveau, B., Chlorovanadates with Original Chain and Layered Structures: Avo_3cl (a = Ba, Sr, Cd). *J. Solid State Chem.* **1999,** *145*, 634-638.
21. Neuefeind, J.; Feygenson, M.; Carruth, J.; Hoffmann, R.; Chipley, K. K., The Nanoscale Ordered Materials Diffractometer Nomad at the Spallation Neutron Source Sns. *Nucl. Instrum. Methods Phys. Rec. Sect. B-Beam Interact. Mater. Atoms* **2012,** *287*, 68-75.
22. Qiu, X. H.; Thompson, J. W.; Billinge, S. J. L., Pdfgetx2: A Gui-Driven Program to Obtain the Pair Distribution Function from X-Ray Powder Diffraction Data. *J. Appl. Cryst.* **2004,** *37*, 678.
23. Farrow, C. L.; Juhas, P.; Liu, J. W.; Bryndin, D.; Bozin, E. S.; Bloch, J.; Proffen, T.; Billinge, S. J. L., Pdffit2 and Pdfgui: Computer Programs for Studying Nanostructure in Crystals. *J. Phys. Condens. Matter* **2007,** *19*, 335219.
24. Momma, K.; Izumi, F., Vesta 3 for Three-Dimensional Visualization of Crystal, Volumetric and Morphology Data. *J. Appl. Cryst.* **2011,** *44*, 1272-1276.
25. Jo, V. K., M.; Shim, I.; Ok, K., Synthesis, Structure, and Characterization of a Layered Mixed Metal Oxychloride, $Pbvo_3cl$. *Bull. Korean Chem. Soc.* **2009,** *30*, 2145-2148.
26. Shannon, R. D. P., C. T., Effective Ionic Radii in Oxides and Fluorides. *Acta Cryst.* **1969,** *B25*, 925.
27. Wangoh, L. M., P. M.; Quackenbush, N. F.; Sallis, S., Fischer, D. A.; Woicik, J. C.; Banerjee, S.; Piper, S. L. J., Electron Lone Pair Distortion Facilitated Metal-Insulator Transition in B-$Pb_{0.33}V_2O_5$ Nanowire. *Appl. Phys. Lett.* **2014,** *104*, 182101-182108.
28. De Jesus, L. R. H., G. A.; Liang, Y.; Parija, A.; Jaye, C.; Wangoh, L.; Wang, J.; Fischer, D. A.; Piper, L. F. J.; Prendergast, D.; Banerjee, S. , Mapping Polaronic States and Lithiation Gradients in Individual V_2O_5 Nanowires. *Nature Commun.* **2016,** *7*, 12021-12029.

29. Velazquez, J. M. J., C.; Fischer, D. A.; Banerjee, S., Near Edge X-Ray Absorption Fine Structure Spectroscopy Studies of Single-Crystalline V_2o_5 Nanowire Arrays. *J. Phys. Chem. C 113*, 7639-7645.
30. Maganas, D. R., M.; Hävecker, M.; Trunschke, A.; Knop-Gericke, A.; Schlögl, R.; Neese, F., First Principles Calculations of the Structure and V L-Edge X-Ray Absorption Spectra of V_2o_5 Using Local Pair Natural Orbital Coupled Cluster Theory and Spin–Orbit Coupled Configuration Interaction Approaches. *Phys. Chem. Chem. Phys.* **2103,** *15*, 7260-7276.
31. Parija, A. W., G. R.; Andrews, J. L.; Banerjee, S. , Traversing Energy Landscapes Away from Equilibrium: Strategies for Accessing and Utilizing Metastable Phase Space. *J. Phys. Chem. C* **2018,** *122*, 25709-25728.
32. Baettig, P.; Seshadri, R.; Spaldin, N. A., Anti-Polarity in Ideal $Bimno_3$. *J. Am. Chem. Soc.* **2007,** *129*, 9854-9855.
33. Seshadri, R.; Hill, N. A., Visualizing the Role of Bi 6s "Lone Pairs" in the Off-Center Distortion in Ferromagnetic $Bimno_3$. *Chem. Mater.* **2001,** *13*, 2892-2899.